Direct Numerical Simulations of a wall-attached cube immersed in laminar and turbulent boundary layers

Carlos Diaz-Daniel, Sylvain Laizet, J. Christos Vassilicos

Department of Aeronautics, Imperial College London, London, SW7 2AZ, UK

Abstract

A wall-attached cube immersed in a zero pressure gradient boundary layer is studied by means of Direct Numerical Simulations (DNS) at various Reynolds numbers Re_H (based on the cube height and the free-stream velocity) ranging from 500 to 3,000. The cube is either immersed in a laminar boundary layer (LBL) or in a turbulent boundary layer (TBL), with the aim to understand the mechanisms of the unsteady flow structures generated downstream of the wall-attached cube. The mean locations of the stagnation and recirculation points around the cube immersed in a TBL are in good agreement with reference experimental and numerical data, even if in those studies the cube was immersed in a turbulent channel. In the TBL simulation, a vortex shedding can be identified in the energy spectra downstream of the cube, with Strouhal number of $St = 0.14$. However, the frequency of the vortex shedding is different in the LBL simulations, showing a significant dependence on the Reynolds number. Furthermore, in the TBL simulation, a low frequency peak with $St = 0.05$ can be observed far away from the boundary layer, at long streamwise distances from the cube. This peak cannot be identified in the LBL simulations nor in the baseline TBL simulation without the wall-attached cube.

Keywords: wall-attached cube, boundary layer, turbulence, Strouhal number

---

*Corresponding authors
Email address:* `c.diaz-daniel13@imperial.ac.uk, s.laizet@imperial.ac.uk,`
`j.c.vassilicos@imperial.ac.uk` (Carlos Diaz-Daniel, Sylvain Laizet, J. Christos Vassilicos)

1. Introduction

The turbulent flow around a wall-attached solid cube represents an interesting and complex problem from a fundamental point of view. Additionally, this flow configuration is a simple model for the interaction between a boundary layer and complex bodies immersed in it. For instance, the wall-attached cube may represent a typical protuberance on the surface of aerodynamic vehicles, such as aircraft or vessels. The flow around low and high aspect-ratio square cylinders is also very important for environmental applications, since it can model the air movement around simplified buildings.

In the last few decades, there has been extensive research on the turbulent flow around wall-attached obstacles with high aspect ratios $H/L \gg 1$ (where H is the obstacle height and L accounts for the base side). Early experiments on the mean-flow characteristics and vortex shedding of high aspect ratio wall-attached circular and square cylinders were performed in the 70's and 80's. Corke et al. (1979) studied the flow near a building model in order to examine the response of the flow field to variations in the characteristics of the boundary layer. Measurements of the vortex-shedding frequency behind a vertical rectangular prism and a vertical circular cylinder attached to a plane wall were performed by Sakamoto & Arie (1983) to investigate the effects of the aspect ratio of these bodies and the boundary-layer characteristics on the vortex-shedding frequency. Kawamura et al. (1984) performed flow visualization experiments and measurements of surface pressure around a finite circular cylinder on a flat plate, in order to study the main flow features close to the immersed objects. More recently, experimental research on the finite-length effects of wall-attached circular and cylinders using hot-wire anemometry was carried out by Park & Lee (2000). Additionally, the Particle Image Velocimetry (PIV) experiments of Wang & Zhou (2009); Monnier et al. (2010); Wang et al. (2014a) provide further insight on the flow structures generated by wall-attached circular and square cylinders. The wind tunnel experiments of Wang et al. (2006) studied the effect of the inflow conditions on the interactions between a boundary layer over a flat plate and flow around a wall-mounted finite-length cylinder.

Finally, the research of McClean & Sumner (2014); Sumner et al. (2015, 2017) focused on the effect of the aspect ratio and the incidence angle of wall-attached objects in a low-speed wind tunnel using PIV.

Direct Numerical Simulations (DNS) of square cylinders were performed by Saeedi et al. (2014) with a study of the turbulent wake behind a wall-mounted square cylinder with aspect ratio 4. Vinuesa et al. (2015) assessed the effect of inflow conditions by considering a fully turbulent zero pressure gradient boundary layer and a laminar boundary layer. The evolution of various flow structures associated with finite length cylinders immersed in a low Reynolds number boundary layer such as wakes, tip vortices, base vortices and horse-shoe vortices were discussed by Saha (2013). A square rectangular tall building was considered by Li et al. (2014) to investigate the effects of turbulence integral length scale and turbulence intensity on the building by means of Large Eddy Simulation (LES). Numerical investigation of the turbulent flow around a surface-mounted square cylinder of aspect ratio 4 were performed by Wang et al. (2014b) to get detailed information about the flow structures around such a cylinder and to establish a suitable turbulent model that could yield accurate and reliable results for practical industrial applications.

The flow around a wall-attached object with $H = L$ is an important classical benchmark for simulations and experiments of bluff bodies. However, there is only a limited number of fundamental studies on the turbulence physics of this flow configuration. The investigation of Castro & Robins (1977) is among the first exhaustive experimental studies on the turbulent flow around a wall-attached cube. The authors compared the effect of uniform and sheared turbulent incoming streams at different Reynolds numbers. Since then, this flow configuration has been revisited, for instance, by the experimental work of Martinuzzi & Tropea (1993) at $Re_H = 40,000$, by Meinders et al. (1999) with $2,750 < Re_H < 4,970$ and by the Direct Numerical Simulation (DNS) of Yakhot et al. (2006b) at $Re_H = 1870$. The scalar concentration field behind a wall-attached cube has been studied experimentally by Ogawa et al. (1983), Li & Meroney (1983) and Mavroidis et al. (2003) at high Reynolds numbers and computationally by

Rossi et al. (2010) at $Re_H = 5,000$, using DNS and Reynolds-Averaged Navier Stokes (RANS) simulations. The recent study of a wall-attached cube by Hearst et al. (2016), at $Re_H = 1.8 \times 10^6$, suggested that different inflow conditions at high Reynolds numbers may not modify the main shedding frequency or the mean position of the stagnation and reattachment points but seem to affect the length of the turbulent wake behind the cube.

The presence of a wall-immersed object in a boundary layer can modify the flow properties in a noticeable way, even with a small blockage ratio. Its turbulent wake induces a momentum loss which results in a rapid increase of the boundary layer thickness. Moreover, despite of its relatively small size, the effect of a wall-attached body on the energy spectra of the flow can persist at long distance from the immersed object. However, there is little fundamental work published on the influence of a wall-attached cube further downstream of its position and on the far-field fluctuations that it generates. On the other hand, the far field dynamics generated by circular and square cylinders are slightly better documented in literature, in particular by the recent works of Becker et al. (2008), King & Pfizenmaier (2009), Porteous et al. (2013) and Moreau & Doolan (2013). An exhaustive review on the far-field dynamics has been recently compiled by Porteous et al. (2014).

The present numerical study investigates the downstream signature of a wall-attached cube, comparing situations where the cube is immersed in a laminar and in a turbulent boundary layer. In particular, we focus on the various peaks found in the energy spectra inside the boundary layer but also at large distances from the wall and far away downstream of the cube. Data in the near-field of the cube are also validated against the reference data of Martinuzzi & Tropea (1993) and Yakhot et al. (2006b).

2. Computational setup

The results presented here have been obtained from high fidelity Direct Numerical Simulations (DNS) of zero-pressure gradient laminar and turbulent boundary layers (LBL, TBL, respectively), with a solid cube immersed in the computational domain.

The baseline simulation of the TBL case, which uses the same numerical domain without the immersed wall-attached cube, was introduced and validated in a fundamental investigation on the wall shear-stress fluctuations by Diaz-Daniel et al. (2017). The local Reynolds number of the TBL covers the range $Re_\theta = 270 - 2,200$, based on the momentum thickness θ and free-stream velocity U_∞.

The computational flow solver, Incompact3d (Laizet & Lamballais, 2009; Laizet & Li, 2011), uses sixth-order finite difference schemes, with a spectral treatment for the pressure equation and a semi-implicit time advancement for the viscous terms. The validation results of the TBL in Diaz-Daniel et al. (2017) include the computation of the budget terms of the mean turbulence kinetic energy equation. The balance of the steady budget terms stays under 1% of the mean dissipation rate in the entire computational domain. The statistics of velocity and wall shear-stress are in excellent agreement with the reference data of Schlatter & Örlü (2010) and Jiménez et al. (2010) at equal Reynolds numbers.

The computational parameters of the present simulations are included in Table 1. The cube height is represented by H and the coordinate variables in the streamwise, wall-normal and spanwise directions are x, y, z, respectively. The coordinate system is shifted to a streamwise position such that $x = 0$ is located at the front plane of the cube. The computational domain is stretched in the wall normal direction using the metric described by Laizet & Lamballais (2009). In the baseline TBL simulation, the mesh resolution, in wall viscous units (at $Re_\theta = 1,470$) is: $\Delta x^+ = 10.2$, $\Delta z^+ = 5.1$, $\Delta y^+ = 0.42$ at the wall and $\Delta y^+ = 108.8$ at the top of the domain. The stretching function parameters guarantee that the wall-normal node spacing inside the boundary layer is lower than $\Delta y^+ = 12$ at the maximum Reynolds number $Re_\theta \approx 2,200$.

The inflow boundary condition in our simulations is a Blasius laminar boundary layer profile prescribed at the inlet plane. In the TBL simulation, the transition to turbulence is triggered via the random-forcing method described in Schlatter & Örlü (2012). A streamwise convective equation is solved at the outlet and a no-slip condition is imposed at the bottom wall. Periodic boundary conditions are used in the spanwise

	Re_θ	$Re_{\delta*}$	$n_x \times n_y \times n_z$	$\frac{L_x}{H} \times \frac{L_y}{H} \times \frac{L_z}{H}$	$\Delta y_{wall}/H$	$\Delta y_{top}/H$	$\Delta t U_\infty/H$	T/H
$Re_H = 500$ LBL	68	175	$357 \times 129 \times 192$	$35 \times 15 \times 8$	0.02	0.68	0.007	10,000
$Re_H = 600$ LBL	81	210	$357 \times 129 \times 192$	$35 \times 15 \times 8$	0.02	0.68	0.007	10,000
$Re_H = 750$ LBL	101	263	$357 \times 129 \times 192$	$35 \times 15 \times 8$	0.02	0.68	0.007	10,000
$Re_H = 1,100$ LBL	149	385	$357 \times 129 \times 192$	$35 \times 15 \times 8$	0.02	0.68	0.007	10,000
$Re_H = 1,700$ LBL	230	596	$357 \times 193 \times 192$	$35 \times 15 \times 8$	0.015	0.41	0.005	10,000
$Re_H = 3,000$ LBL	406	1,051	$513 \times 385 \times 256$	$35 \times 15 \times 8$	0.007	0.22	0.002	3,000
$Re_H = 3,000$ TBL	750	1,105	$4,097 \times 513 \times 256$	$320 \times 27 \times 10$	0.0033	0.833	0.001	750

Table 1: Summary of the simulation parameters (the momentum thickness is θ and the displacement thickness is $\delta*$) for the present investigation.

direction, effectively modelling an infinite array of cubes, and an homogeneous Neumann condition is imposed at the top boundary.

The solid cube, of size H, is modelled with an immersed boundary method (see Laizet & Lamballais (2009) for the details). In the simulation with an incoming TBL, the height of the cube, H, is equal to 0.42δ, where δ is the local boundary layer thickness, and the Reynolds number based on H and U_∞ is $Re_H = 3,000$. The cube is placed at a streamwise distance of $72H$ from the inlet, where the local Reynolds number is $Re_\theta = 750$. At the cube's top face location, $y = H$, the wall-normal stretching function satisfies $\Delta y^+ = 0.82$. In the simulations with an incoming LBL, the cube has a height $H = \delta$ and is located at a distance $9H$ from the inlet. Six different Reynolds numbers are simulated, $Re_H = 500, 600, 750, 1,100, 1,700$ and $3,000$. The value of δ/H guarantees that the ratio between the local displacement thickness of the boundary layer and the cube height is similar in the LBL and TBL simulations, being respectively $\delta*/H = 2.86$ and $\delta*/H = 2.7$. The blockage ratio of the cube, based on the frontal area of the obstacle and the total area occupied by δ, is $\sigma = 4.2\%$ in the TBL simulation and $\sigma = 12.5\%$ in the LBL simulations.

The statistics presented in this study have been averaged over a time period T indicated in Table 1, after letting the simulations run for a sufficiently long initial transient period. For the computation of the energy spectra, the time signals were split and averaged over windowed intervals (using a Hanning window) with 50% overlap.

The number of windowed intervals is 40 in the LBL simulations up to $Re_H = 1,700$, 20 in the LBL simulation at $Re_H = 3,000$ and 2 in the TBL simulation. The non-dimensional power spectral density (PSD) has been defined as $PSD_{u_i} = E_{u_i u_i} U_\infty^{-1} H^{-1}$, where $E_{u_i u_i}$ is the temporal energy spectrum of the velocity component u_i.

3. Wall-attached cube under laminar upstream conditions

The focus in this section is on the coherent structures generated by a cube under laminar upstream conditions for Reynolds numbers ranging from 500 to 3,000. According to the results of Meinders et al. (1999) and Yakhot et al. (2006b), the mean flow topology and dynamics seem to be approximately Reynolds number independent for $Re_H > 2,000$ when the incoming boundary layer is fully turbulent. Therefore, the results at $Re_H = 3,000$ under TBL upstream conditions are expected to be representative of higher Reynolds numbers cases.

3.1. Mean flow topology

Previous computational studies of a wall-attached object immersed in a channel for Reynolds numbers ranging from 0.01 to 3,500 suggested that the mean-flow topology around a wall-attached cube under LBL conditions is strongly dependent on the Reynolds number, at least up to $Re_H < 2,000$ (Liakos & Malamataris, 2014; van Dijk & de Lange, 2007; Hwang & Yang, 2004). The location of the main mean-flow features obtained in our simulations are summarised in Table 2. The last row presents the results for a cube under TBL conditions (see section 4 for a detailed discussion).

For $Re \leq 1,700$, the mean-flow streamlines behind the cube, shown in Figure 1, do not create a closed recirculation region. However, there exists a stagnation point, marked D' in Figure 1, which is located at closer distance $x_{D'}$ from the cube for increasing Reynolds numbers. In the simulation at $Re_H = 3,000$, a recirculation point can be found at $x_D = 1.63H$, $y_D = 1.11H$ (point D in the bottom plot of Figure 1), in addition to the stagnation point D'. For $Re \leq 3,000$, no recirculation region can

7

	Front face. stag. y_A	Stag point $x_{D'}$	Stag point $y_{D'}$	Stag. point x_F	Recirc. point x_D	Recirc. point y_D
$Re = 500$	0.82	3.48	0.17	-1.6	-	-
$Re = 600$	0.82	3.22	0.21	-1.7	-	-
$Re = 750$	0.82	2.98	0.24	-1.8	-	-
$Re = 1,100$	0.82	2.19	0.145	-2.0	-	-
$Re = 1,700$	0.81	2.15	0.141	-2.25	-	-
$Re = 3,000$	0.81	1.93	0.181	-2.57	1.63	1.11
$Re = 3,000$ (turb.)	0.67	-	-	-1.4	1.45	0.87

Table 2: Positions of the mean flow features of a wall-attached cube with a laminar incoming boundary layer. In the last row, we have added, for comparison, the results of the simulation with incoming TBL at $Re_H = 3,000$, described in Section 4.

be found over the top surface of the cube but the mean-flow streamlines are strongly curved over the cube due to a strong backflow in the streamwise direction.

The upstream stagnation point (point F in Figure 1) moves farther from the front face with increasing Reynolds numbers. On the other hand, its streamwise position x_F has been reported to be approximately constant when the flow around the cube becomes fully turbulent (Yakhot et al., 2006b). An empirical correlation for the position of this stagnation point in the range $300 < Re_H < 1,500$ was proposed by Hwang & Yang (2004), $x_F/H = -0.77 \log(Re_H) + 0.564$, measured on the x-z plane $y = 0.006H$. In our simulations, the location of the upstream stagnation point measured at the plane $y = 0.025H$ (x_F in Table 2), also follows a logarithmic trend for $500 < Re_H < 3,000$, $x_F/H = -1.24 \log(Re_H) + 1.77$ (see Figure 2(a)). The 10-15% difference with the correlation predictions of Hwang & Yang (2004) can be attributed to the different set-up (channel flow of size $2H$ versus boundary layer).

The horseshoe vortex system observed just upstream of the cube is stable for all our laminar simulations. The work of Baker (1979) investigated the horseshoe vortex system around high-aspect ratio cylinders for different flow conditions, and suggested that its topology and stability depend mostly on the Reynolds number and the ratio D/δ^*, where D is the cylinder diameter and δ^* is the boundary layer displacement
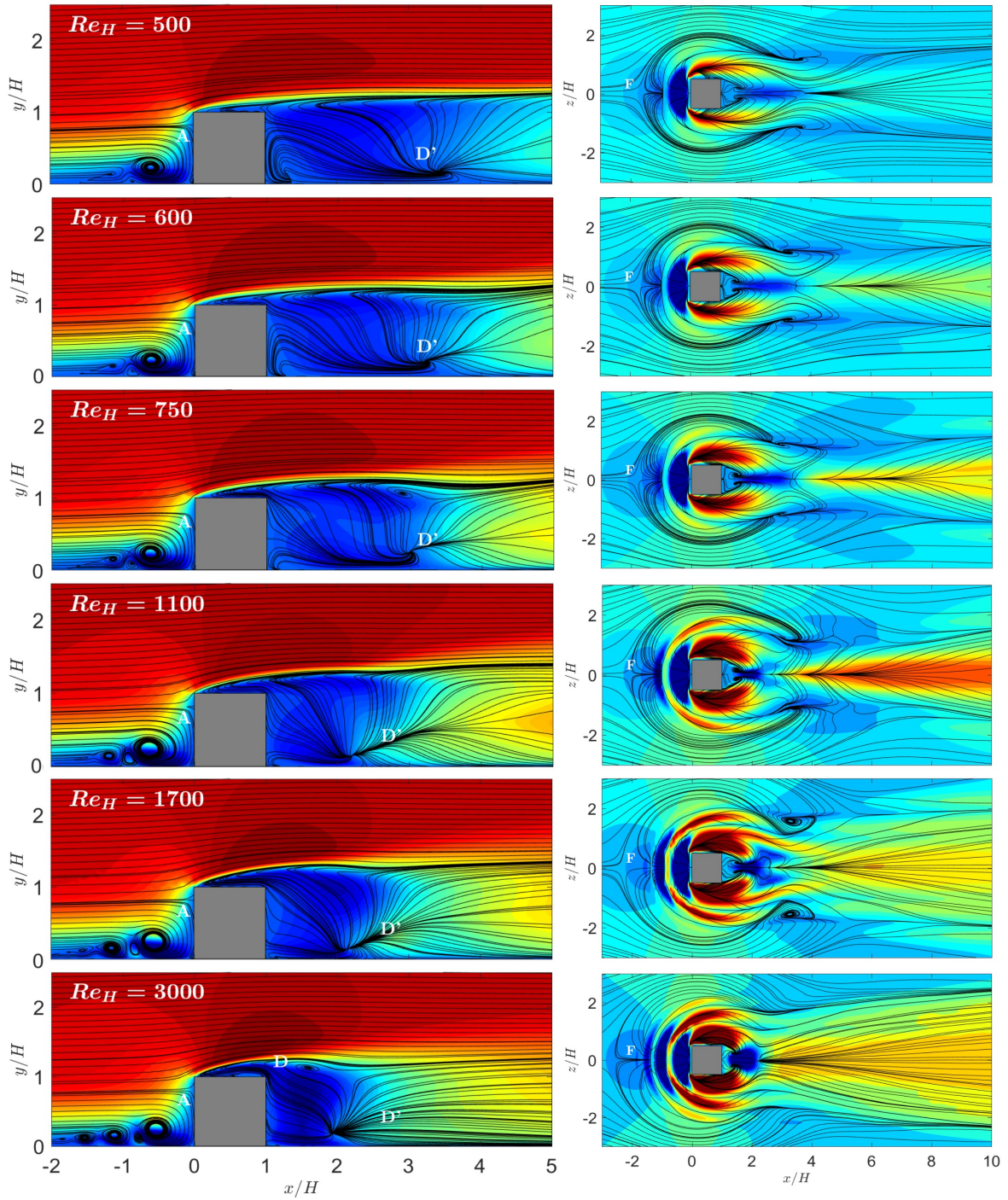
8

Figure 1: Mean flow streamlines and time-averaged streamwise velocity contours around a wall-attached cube at different Reynolds numbers. Left: x-y plane $z = 0$ (the colourmap for $\overline{u}$ ranges from $-0.1U_\infty$, dark blue, to $1.1U_\infty$, dark red). Right: x-z plane $y = 0.025$. (colourmap for $\overline{u}$ from $-0.1U_\infty$, dark blue, to $0.2U_\infty$), dark red.

thickness. Depending on the pair of dimensionless numbers $\{Re_D, D/\delta^*\}$ (Re_D is based
on the cylinder diameter), the horseshoe vortex system may be either stable with 2,
4 or 6 vortices, or unstable following a quasi-periodic behaviour. The stability map
obtained from the experiments on cylinders by Baker (1979) is presented in Figure 2(b).
Our simulations have been included in this map for reference, based on their values of
$\{Re_H, H/\delta^*\}$. The different vortex systems from our simulations can be identified in
the streamline visualisations of Figures 1 (stable vortices) and 6(a) (unstable vortex,
see Baker (1979) for a more detailed description).

(a)   (b)
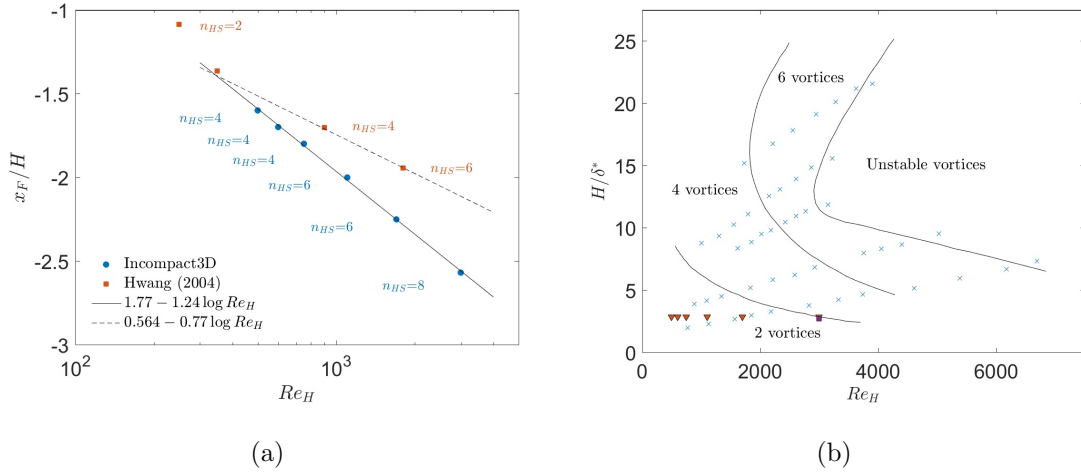
Figure 2: **a)** Position of the upstream stagnation point generated by a wall-attached cube under laminar
inflow conditions. In Hwang & Yang (2004), it is measured in a channel at a distance $y = 0.006H$
from the wall, while in the current simulation it was measured in an LBL at $y = 0.025H$ from the
wall. The value n_{HS} indicates the number of steady horseshoe vortex found at each Reynolds number.
b) Dependency of the horseshoe system dynamics on the parameters Re_D and D/δ^* for the wall-
attached cylinder experiments of Baker (1979), indicated with blue cross symbols. The continuous
lines indicate the empirical threshold between the 2-vortex, 4-vortex, 6-vortex and unstable horseshoe
systems obtained by these authors. The triangles and the square represent the pairs Re_H and H/δ^* in
our cube simulations under LBL and TBL upstream conditions, respectively. Note that the numbers
of horseshoe vortices found in these simulations are different than those predicted by the diagram for
cylinders proposed by Baker (1979).

In Figure 2(a), the position of the stagnation point is plotted for the present sim-
ulations and for the work of Hwang & Yang (2004), indicating the number of steady

horseshoe vortices found for each case. The ratio H/δ^* is different in both investi-gations, with a value of 2.8 in our study and a value of 1 in Hwang & Yang (2004). According to the stability map of Baker (1979) in Figure 2(a), the horseshoe vortex system around wall-attached cylinders should consist of 2 vortices with a low ratio H/δ^* and Re_H between 500 and 1,700. However, in the present simulations, the horseshoe vortex system contains 4 steady vortices approximately for $300 < Re_H < 1,000$, 6 vor-tices for $1,000 < Re_H < 3,000$ and 8 vortices for $Re_H \geq 3,000$ and a similar behaviour is inferred from the results of Hwang & Yang (2004). At $Re_H = 3,000$, the horseshoe system remains stable even if some unsteady fluctuations are noticeable. This suggests that the stability limits can be significantly different depending on the geometry of the wall-attached objects.

In contrast to the Reynolds number dependence of the topological features discussed in the previous paragraph, the position of the stagnation point on the cube front face (A in Figure 1) is approximately constant for the range $Re_H = 500 - 3,000$, at $y_A = 0.82$. Finally, the mean-flow streamlines suggest that the wake behind the cube becomes wider for increasing Reynolds numbers. In the low Reynolds number simulations, $Re_H = 500, 600, 750$, the streamlines in the cube wake are almost parallel to the streamwise direction for $|z| > 1.4H$, $x > 6H$. This suggests that the wake width at low Reynolds numbers is approximately constant, with value $W_{wake} = 2.8H$.

3.2. Dynamic structures

Instantaneous visualisations from the LBL simulations at $Re_H = 500 - 3,000$, using the Q criterion (defined by Hunt et al. (1988)), are presented in Figures 3 and 4. These visualisations suggest that the coherent velocity fluctuations may be associated with a periodic generation of hairpin vortices from the top of the cube. The two upper side edges induce vortical motions, which presumably interact with the shear layer created over the cube and this may lead to flow instability. This mechanism creates a primary street of symmetric hairpin vortices, which are detached from the wall. For low Reynolds numbers ($Re_H = 500 - 750$), vortex generation starts farther downstream

11

of the cube than for higher Reynolds numbers.

At $Re_H = 500$, the isocontours of $Q = 0.1U_\infty^2/H^2$ 3(a) do not show any unsteady structure since the velocity fluctuations are very low. If the threshold for Q is relaxed down to $Q = 0.003U_\infty^2/H^2$ (drawn with low opacity), weakly unsteady structures are revealed, which develop into hairpin vortices at $x > 15H$. Therefore, this suggests that the critical Reynolds number for flow unsteadiness may be close to $Re_H = 500$. According to the flow visualisations, the hairpin vortices might be related to an instability mechanism of the steady streamwise vortices which are generated at the cube top edges.
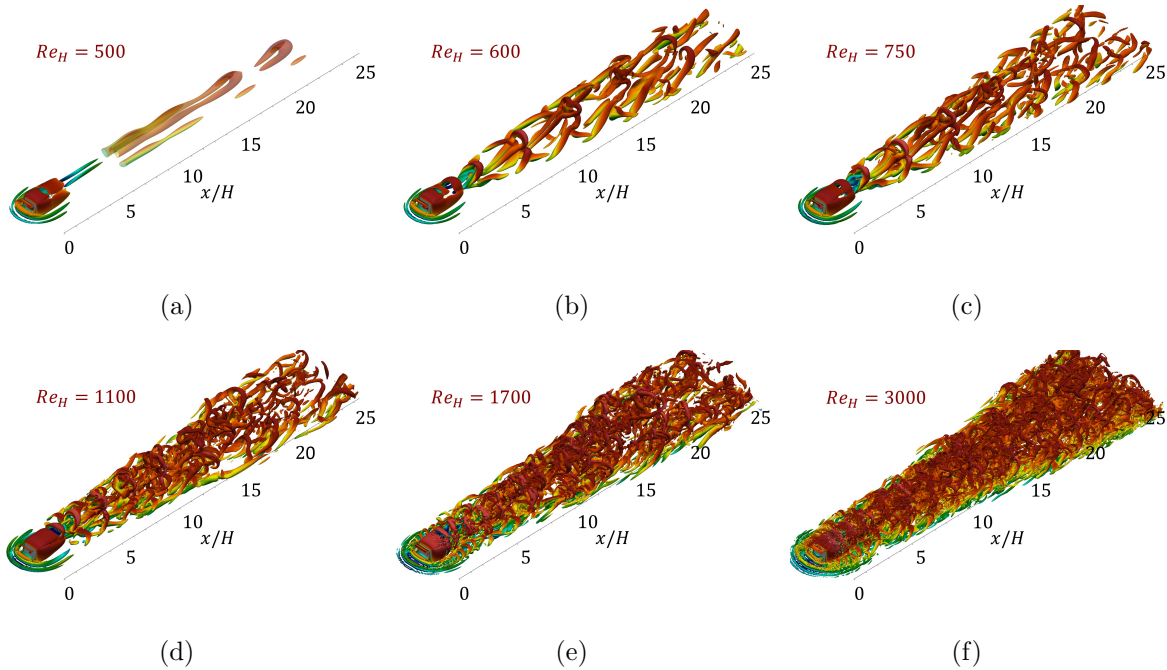
Figure 3: Simulation of a wall-attached cube at different Reynolds numbers with a laminar incoming boundary layer. **a,b,c)** Isocontours of $Q = 0.1U_\infty^2/H^2$, coloured by streamwise velocity (from $-0.5U_\infty$, in dark blue, to $1.1U_\infty$, in dark red). **d)** Isocontours of $Q = 0.2U_\infty^2/H^2$ and **e,f)** isocontours of $Q = 0.28U_\infty^2/H^2$. In subfigure **(a)**, the low opacity surface represents the isocontour $Q = 0.003U_\infty^2/H^2$.

The Strouhal number associated with the hairpin vortex structures at $Re_H = 500$ is $St = 0.17$. The unsteady structures appear as a single sharp and intense peak in the turbulence energy spectra, which is shown for different downstream locations in Figure 4(a). These energy spectra have been averaged over 9 equidistant spanwise locations

12

between $z = -1.5H$ and $z = 1.5H$ from the cube centre plane. The obtained value $St = 0.17$ is in good agreement with the Strouhal number obtained by the DNS of Yanaoka et al. (2007) at $Re_H = 500$ ($St = 0.159$). The coherent velocity fluctuations are significantly stronger in Yanaoka et al. (2007), where symmetry conditions were used in the spanwise direction and a slip condition on the domain top plane, located at $y = 10H$ from the wall. These authors reported that the flow solution in their simulation at $Re_H = 450$ is stable, which supports our previous statement suggesting that $Re_H = 500$ may be close to the critical value for unsteady flow.

In the present simulations, the magnitude of the peak found in the energy spectra is maximum around $x = 15H$, $y = H$ from the cube, after the shear layer becomes unstable. When moving farther downstream at $y = H$, the peak intensity is reduced, but can still be detected up to the domain outlet. The magnitude of the peak in the power spectra reported by Yanaoka et al. (2007) (measured at $y = H$) also decreases for increasing $x > 6H$.

For $Re_H = 600$, the contours of Q suggest that another two streets of hairpin vortices, which are attached to the wall, are generated on the sides of the primary structures, possibly from a secondary interaction between the cube flow structures and the wall. These secondary vortex streets are symmetrically separated by a distance of approximately $1.2H$ from the cube centre plane $z = 0$. Their generation may be associated with the instabilities caused by the vortical motion of the horseshoe vortex legs. In particular, the flow region around a horseshoe vortex is fundamentally similar to a quasi-streamwise vortex from the near-wall region of a turbulent wall-bounded flow. Therefore, it might be reasonable to expect similar hairpin-vortex structures to those discussed by Adrian (2007) for the buffer and log layers.

The Strouhal number of the primary top vortices, $St = 0.19$, is slightly increased in comparison to the $Re_H = 500$ case. The secondary wall-attached structures are shed at the same frequency, but the interaction between the different structures seems to result in harmonic peaks at $St = 0.38$, $St = 0.57$ and higher multiples of the main Strouhal number $St = 0.19$. The interaction with the wall and between the vortex streets may
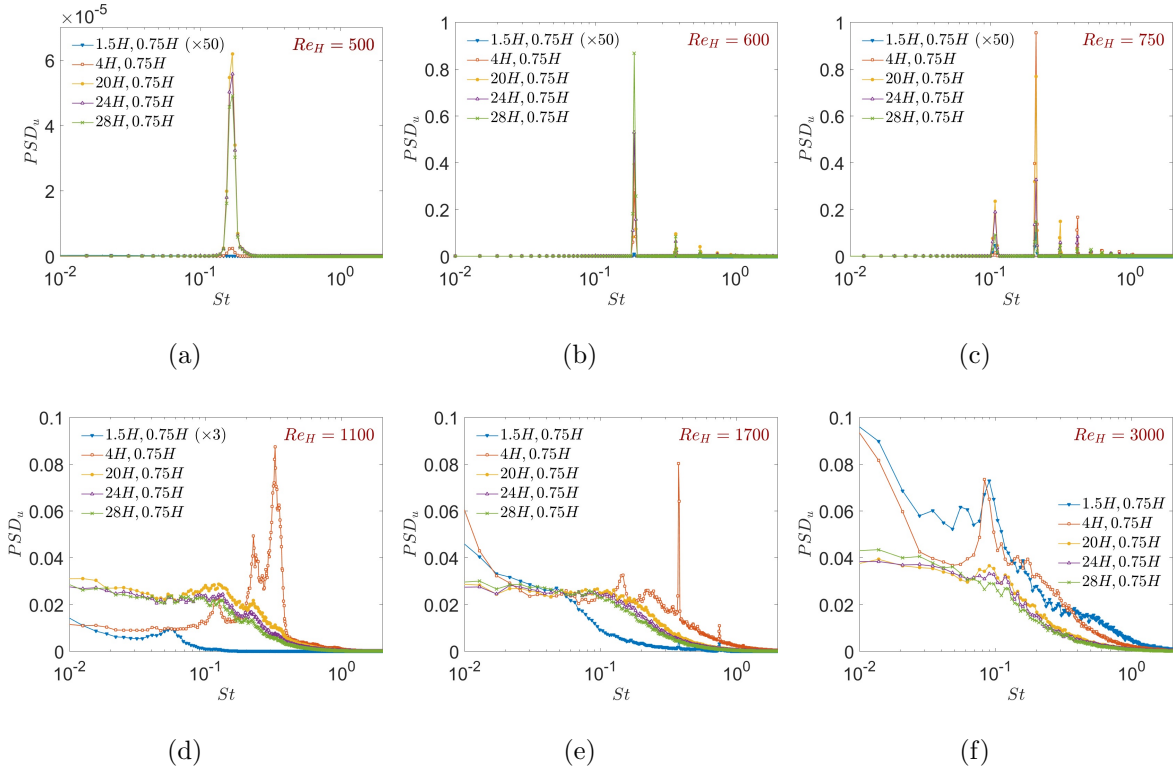
13

Figure 4: Simulation of a wall-attached cube at different Reynolds numbers with a laminar incoming boundary layer. Energy spectra of the streamwise velocity component u at different positions x, y. The power-spectral density (PSD) has been non-dimensionalised as $PSD_u = E_{uu}U_\infty^{-1}H^{-1}$.

also be responsible for an amplification of the primary peak in the energy spectra, since its magnitude keeps increasing when moving away from the cube.

At $Re_H = 750$, stronger flow interactions between the cube and the wall produce a higher number of secondary structures and a more disorganised distribution of them. The Strouhal number of the main shedding further increases to $St = 0.21$. The vortex interaction and additional flow instabilities behind the cube generate a secondary peak with a lower Strouhal number $St = 0.1$. This peak can be associated with a new phenomenon since the harmonics found at $Re_H = 600$ all have higher frequencies than the main peak. The interaction between the new peak at $St = 0.1$ and the primary peak at $St = 0.21$ also generates the harmonic $St = 0.1 + 0.21 = 0.31$. Interestingly, the velocity fluctuations at $St = 0.1$ for this Reynolds number seem to be less amplified

14

than in the $Re_H = 600$ case. At $Re_H = 750$, the primary peak reaches its maximum magnitude around $x = 4H$ and decreased downstream of this location.

The vortex visualisations presented in Figure 3(d) suggest that, at $Re_H = 1,100$, the flow structures are much more complex than in the previous cases, but it is still possible to distinguish the vortical structures described before. The primary hairpin vortex street can be found close to the cube, but after a short distance away from the cube, the interaction with other flow structures becomes very strong and the vortices break down into less organised motions. The secondary streets of wall-attached hairpin vortices on the sides of the cube can be identified as well.

The near-cube coherent structures are shed with higher frequency than at lower Reynolds numbers and the Strouhal number of the main peak in the energy spectrum computed at $x = 4H$, $y = 0.75$ is equal to $St = 0.32$. However, secondary peaks at $St = 0.22$ and $St = 0.12$ are also identified, which might be the signature of the coherent fluctuations found at lower Reynolds numbers. The energy spectra suggest that the flow interactions at $Re_H = 1,100$ are non-linear and that the flow may become turbulent further downstream of the cube. At this Reynolds number, the turbulent kinetic energy is distributed in a broad band range of frequencies and no peaks can be easily identified for $x > 20H$ and $y < H$. It is interesting to note that a low frequency peak, with $St = 0.05$, can be found in the energy spectrum at $x = 1.5H$. It seems that this low frequency peak is only detected inside the backflow region behind the cube (see Figure 1), suggesting that the flow dynamics may be different here. The peak at $St = 0.05$, weak in comparison with the other ones, is not present in the spectrum at $x = 4H, y = 0.75H$ nor for higher streamwise positions.

At $Re_H = 1,700$, the main peak with $St = 0.32$ found at $Re_H = 1,100$ and $x = 4H$ can also be identified, but its Strouhal number increases to $St = 0.37$. While the peak at $St = 0.22$ is much weaker at $Re_H = 1,700$, the peak at $St = 0.14$ has a greater magnitude than the peak at $St = 0.12$ at $Re_H = 1,100$. Since the Strouhal number is the same as the one identified in the simulation with a turbulent incoming boundary layer in Figure 10(a), the peaks found at $St = 0.14$ for $Re_H = 1,700$ and $Re_H = 3,000$

15

might possibly be associated with the same flow structures. Hwang & Yang (2004) stated that the mechanism which generates the dominant peak with $St \approx 0.12 - 0.14$ at high Reynolds numbers is not well understood, since the main coherent structures are shed with higher Strouhal numbers. However, these authors suggested that the peak at $St \approx 0.13$ actually dominates the force coefficient of the total spanwise loading on the cube. While the horseshoe vortex is still stable at $Re_H = 1,700$, the isocontours of Figure 3(e) show a strong generation of hairpin vortices around its legs. The shedding of hairpin vortices can be related to a new peak with $St = 0.75$ found in the energy spectra, since these are the only coherent structures found to be shed at such high frequencies. At higher downstream distances from the cube, the energy spectra at $St = 1,700$ does not predict any dominant peak, only broadband fluctuations.

At $Re_H = 3,000$, a single peak with $St = 0.1$ can be identified in the energy spectra of Figure 4(f) at $x = 1.5H$ and $x = 4H$, but it is no longer detected far downstream. The horseshoe vortex system is stable, and the instantaneous and averaged streamlines in front of the cube are very similar to each other. However, Figure 5(a) shows that the largest horseshoe vortices are not steady and they generate weak velocity fluctuations which can be associated to a peak in the energy spectra found at approximately $St = 0.085$, as seen in Figure 5(b). The St value is relatively similar to the one reported in Yakhot et al. (2006a) for the unstable horseshoe vortex system of a cube under turbulent upstream conditions ($St \approx 0.08$), suggesting that the velocity fluctuations in the two cases might be related to the same physics.

Finally, the far-field velocity signature of the cube at $Re_H = 3,000$ is also presented in Figure 5(b). The turbulence energy spectra suggests that the signature of the coherent motions detected near the cube is not noticeable far downstream of the cube location. At $y = 3H$ and $x > 20H$, the energy is spread in a broad bandwidth of frequencies, centred around $St = 0.15 - 0.2$, and no sharp peak can be observed. The results suggest that the main frequency of the excited region of the energy spectra may decrease for increasing values of x/H.
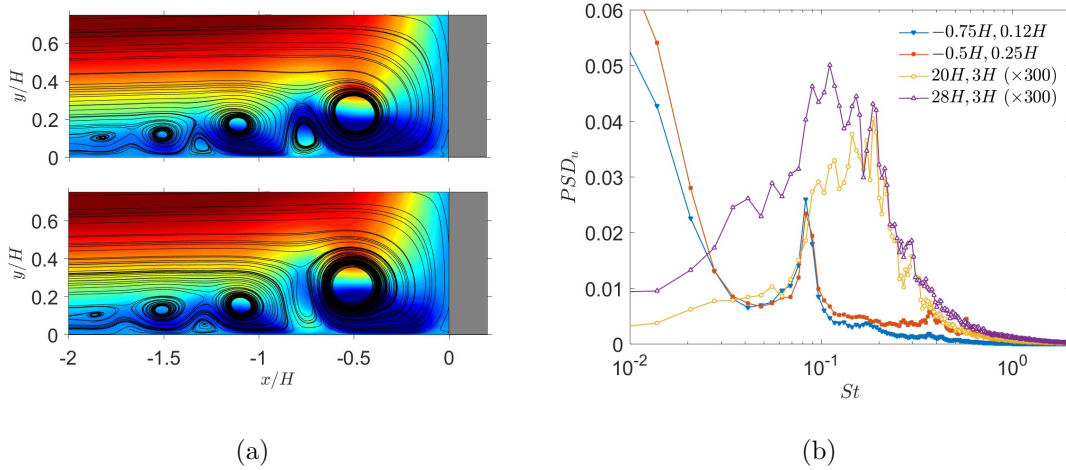
Figure 5: Simulation of a wall-attached cube at $Re_H = 3,000$ with a laminar incoming boundary layer: **a)** Instantaneous contours of the streamwise velocity component and instantaneous streamlines on the x-y plane $z = 0$. Detail of the front horseshoe vortex. **b)** Energy spectra of the streamwise velocity component u at the front horseshoe vortex position and in the cube far-field. The non-dimensional PSD is defined as $PSD_u = E_{uu}U_\infty^{-1}H^{-1}$.

4. Wall-attached cube under turbulent upstream conditions

4.1. Mean-flow features in the near-cube region

The mean flow features of our TBL simulation at $Re_H = 3,000$ are compared with published experimental and simulation data (Martinuzzi & Tropea, 1993; Yakhot et al., 2006b). In those studies, the Reynolds number Re_H is similar to ours, but the cube is immersed in a turbulent channel instead of a turbulent boundary layer. The mean flow streamlines in Figures 6(a) and 6(b) show the time averaged structures around the cube. In the centre plane $z = 0$, the stagnation point A is located at $y_A/H = 0.67$, the reattachment point E at $x_E/H = 2.5$, the front vortex C has its centre at $x_C/H = 0.48$ and the horizontal location of the rear recirculation centre D is $x_D/H = 1.45$. Those spatial positions are in good agreement with the numerical results of Yakhot et al. (2006b), with differences of less than 3%. On the other hand, the location of the top recirculation bubble B, $x_B/H = 0.65$ and $y_B/H = 1.13$, and the vertical position of the rear recirculation D, $y_D/H = 0.87$, have a 10-15% relative error with respect to

17

the values found in Yakhot et al. (2006b). This can be explained by the different top boundary condition, since the upper wall in the channel configuration constraints the flow in the vertical direction.

The results are summarized in Table 2 and the comparison with Figure 1 shows important disparities in the location and size of the mean-flow features between simulations under LBL and TBL conditions for the same Reynolds number. For instance, the distance from the mean stagnation point and the cube front face, x_F, is 45% lower for the TBL simulation and the location of the stagnation point A on the cube front face is lower by 17% with $y_A = 0.67$. The authors in Vinuesa et al. (2015) have also previously reported that the inflow conditions can have an important influence on the main flow features around a high aspect-ratio square cylinder. It was suggested that, while the Strouhal number of the main shedding is approximately the same ($St = 0.1$) under incoming turbulent and laminar upstream conditions, the upstream horseshoe vortex dynamics and the downstream wake parameters may be significantly different.

The TBL simulation at $Re_H = 3,000$ exhibits an unstable horseshoe vortex system in front of the cube, as confirmed by the mean-flow streamlines in Figure 6(a), and in agreement with the results reported by Yakhot et al. (2006a). It seems that the dynamics of this flow feature are strongly dependent on the turbulence upstream conditions, as suggested by Baker (1979) with a dependence with the parameters Re_H and δ^*/H only. The LBL and TBL simulations at $Re_H = 3,000$ have more or less the same value of $\delta^*/H \approx 2.8$ but the horseshoe vortex dynamics and the main mean-flow features around the cube are fundamentally different. On the other hand, similar results obtained in the present simulation and in Yakhot et al. (2006b) suggest that the effect of the top boundary condition (TBL versus turbulent channel) is not that important for this flow feature.

Periodic boundary conditions in the spanwise direction are modelling an infinite array of cubes and one can average the flow variables over $[-L_z/2, L_z/2]$ to estimate the effect of the cube on the boundary layer statistics. The interaction with the cube increases the span-averaged momentum thickness by a constant $\Delta\theta$, which is reflected
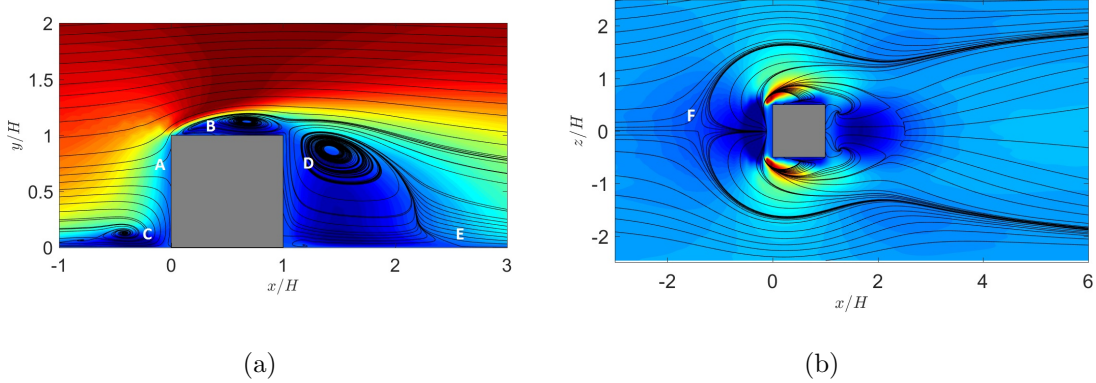
18

Figure 6: **a)** Mean velocity streamlines in the spanwise plane $z = 0$. Coloured contours by velocity magnitude (from -0.25, blue, to $1.1U_\infty$, red). **b)** Mean velocity streamlines in the wall-normal plane $y/H = 0.0045$. Coloured contours by streamwise velocity (from $-0.1U_\infty$, blue, to $0.2U_\infty$, red).

in the Reynolds number, as shown in Figure 7(a). By using the physical meaning of the momentum thickness, $D = U_\infty^2 L_z \Delta\theta$, the drag coefficient of the cube can be related to $\Delta\theta$ as $C_d = 2\Delta\theta L_z/H^2 = 2\frac{\Delta Re_\theta}{Re_H}\frac{L_z}{H} = 0.7$. The obtained value of the drag coefficient, $C_d = 0.7$, is in good agreement with the result obtained by integrating the surface forces, equal to $C_d = 0.72$ (the contribution of the pressure forces on the front and rear faces to the form drag is 0.642 and 0.09 respectively, and the skin friction drag only contribute as -0.011, a 1.5% of the total). Differences in the drag coefficient with the experiments of Martinuzzi & Havel (2004) ($C_d \approx 0.95$) can be attributed to different incoming flow conditions which affect the cube wake characteristics (in their study, a Blasius laminar profile with $\delta/H = 0.07$ was prescribed upstream of the cube). The experimental studies of Sakamoto et al. (1982) and Sakamoto & Oiwake (1984) suggest that the drag coefficient of the cube strongly depends on the ratio H/δ. These authors obtained a value around $C_d \approx 0.4$ for $H/\delta = 0.15$, a value around $C_d = 0.6$ for $H/\delta = 0.5$ and $C_d = 0.95$ for $H/\delta = 1.5$.

Moving further downstream, the span-averaged velocity profiles recover a canonical state for the inner and buffer regions of the TBL and the influence of the cube is mostly concentrated on the inertial and wake layers. The comparison between the span-averaged turbulent fluctuation profiles at $Re_\theta = 1,000$ (22.3H downstream of

19

the cube), presented in Figure 7(b), shows a significant increment for span-averaged streamwise fluctuations expressed in wall units u_{rms}^+ in the cube simulation between $y^+ \approx 80$ and $y^+ \approx 300$, while the inner part of boundary layer remains unaltered. Thus, the effect of the immersed cube on the the span-averaged turbulence statistics is mostly concentrated around its upper edges, located at $y^+ \approx 132$.
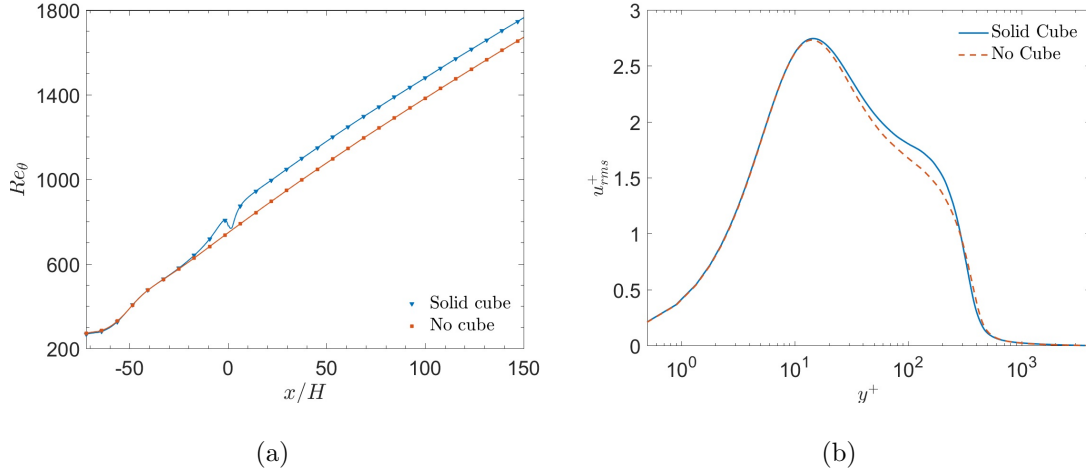

(a)   (b)

Figure 7: **a)** Effect of the cube on the span- averaged momentum thickness. **b)** Effect of the solid cube in the span-averaged streamwise fluctuations, at $Re_\theta = 1,000$. This Reynolds number location can be found at $111H$ in the unperturbed boundary layer simulation and at $95H$ in the cube simulation ($22.3H$ downstream of the cube).

4.2. Energy spectra inside the boundary layer

In the near-field flow around the cube, for $y < H$, top, rear and lateral recirculations shed unsteady vortices, producing a dominant peak in the velocity spectra. Previous studies have reported a shedding frequency with a Strouhal number $St = fH/U_\infty = 0.08 - 0.15$ (Yakhot et al., 2006b; Porteous et al., 2014; Martinuzzi & Havel, 2004). In our simulation, close to the rear wall of the obstacle ($x = 4.7H, y = 0.73H, z = 0$), it is possible to identify a peak in the turbulence spectra with $St = 0.14$ as seen in Figure 8(a). The peak frequency lies within the range of values found in the literature and is in good agreement with the empirical correlation of Wang & Lu (2012), based on experimental results. Further downstream, the peak in the energy spectra of the

20

streamwise component u is masked by the boundary layer turbulence and cannot be detected for $y < \delta$ (see Figure 8(a) for $x = 36H$). The spectra of the spanwise component w also presents a peak with $St = 0.14$ which is shown in figure 8(b). While the magnitude of this peak decreases further downstream, it is still noticeable at $y/H = 36$, as the background spanwise fluctuations of the boundary layer are less intense than the streamwise ones.
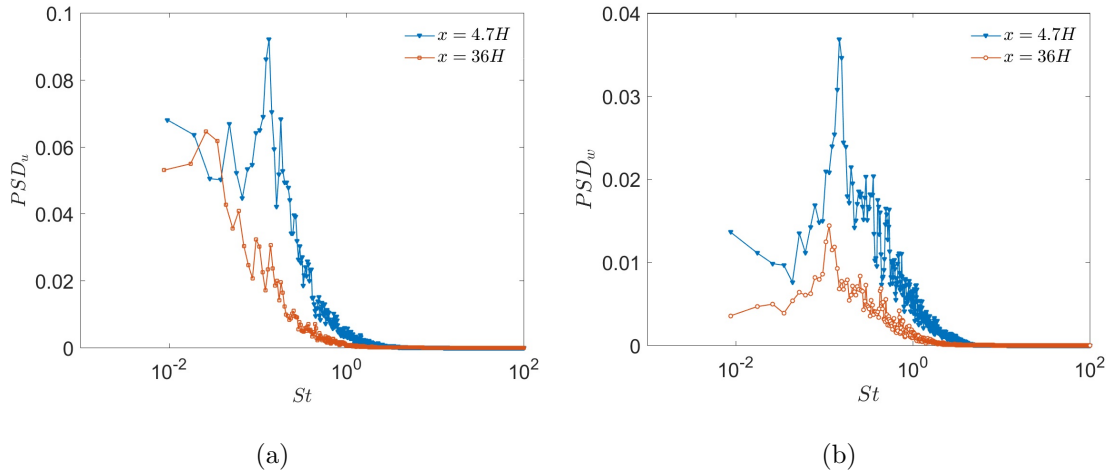

(a) (b)

Figure 8: Energy spectra of **a)** streamwise and **b)** spanwise velocities in the near field of the wall-attached cube, at $y = 0.73H$ and $z = 0$. Comparison at $x = 4.7H$ and $x = 36H$ downstream of the cube (points P and P' in Figure 9). The non-dimensional PSD is defined as $PSD_{u_i} = E_{u_i u_i} U_\infty^{-1} H^{-1}$.

4.3. Energy spectra outside the boundary layer

In the free-stream, away from the boundary layer, an array of virtual probes recorded the velocity signal as a function of time at different streamwise positions and same distance from the wall, $y/H = 4.7$, as sketched in Figure 9. In this region, the flow statistics have small variations in the spanwise direction and, thus, the frequency spectra have been averaged over 16 equally-spaced spanwise positions to improve statistical convergence. Far away from the boundary layer (at least $y/H = 3 - 4$ from the wall), a sharp peak with Strouhal number $St = 0.05$ is found in the turbulence spectra for large distances downstream of the cube, around $x/H > 30$ (Figure 10(a)). The peak magnitude is low since this position is far from the turbulent region, but it is over 5 times

21

higher than the magnitude obtained in the simulation with no cube at the exact same spatial locations. The shape of the far-field spectra generated by the baseline turbulent

420 boundary layer is similar to the one obtained experimentally by Favre et al. (1957), and may be explained by the theoretical model of irrotational fluctuations by Philips (1955). The free-stream spectra of a TBL was briefly discussed again by Rodríguez-López et al. (2016).
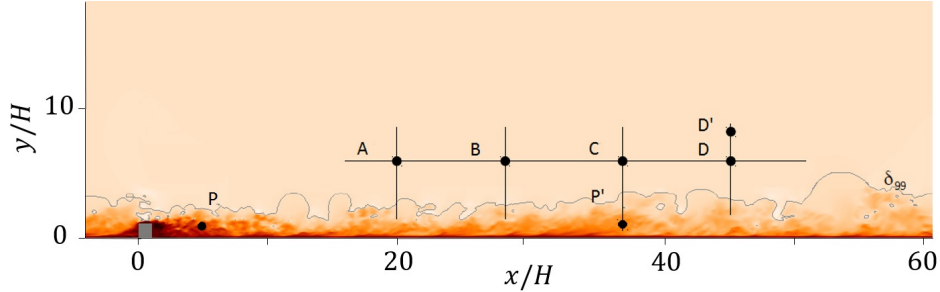

Figure 9: Probe positions for the frequency spectra in the wall-attached cube simulation. Points P, P': inside boundary layer, $x/H = 4.7, 36$, $y/H = 0.7$. Points $A - D$, free-stream far-field, $y/H = 4.7$ and $x/H = 20, 28, 36, 45$; D' at $y/H = 6.5$, $x/H = 45$.

Figure 10(b) shows that, at an equal distance $y/H = 4.7$ from the wall, peak

425 magnitudes in the cube simulation's span-averaged streamwise spectra increase with downstream distance, but the peak frequency does not change. This suggests that the fluctuations created by the cube may propagate and possibly amplify downstream and upwards. This effect could be associated with the boundary layer thickness growth, but the value of the energy spectra peak measured at $x = 20H, y = 4.7H$, located at $2.3H$

430 from the boundary layer edge, is lower than the peak value measured at $x = 45H, y = 6.5H$, at $2.9H$ from the boundary layer edge. The frequency of the peak is very low and cannot be associated directly with the vortex shedding of the cube measured closer to the wall. Note that in previous experimental studies of round and square cylinders by Porteous et al. (2013) and Porteous et al. (2014), a low-frequency peak was also

435 detected in the far-field with $St = 0.07$. The authors associated this peak with the tip flow shedding, occurring at a different frequency from the main vortex shedding with
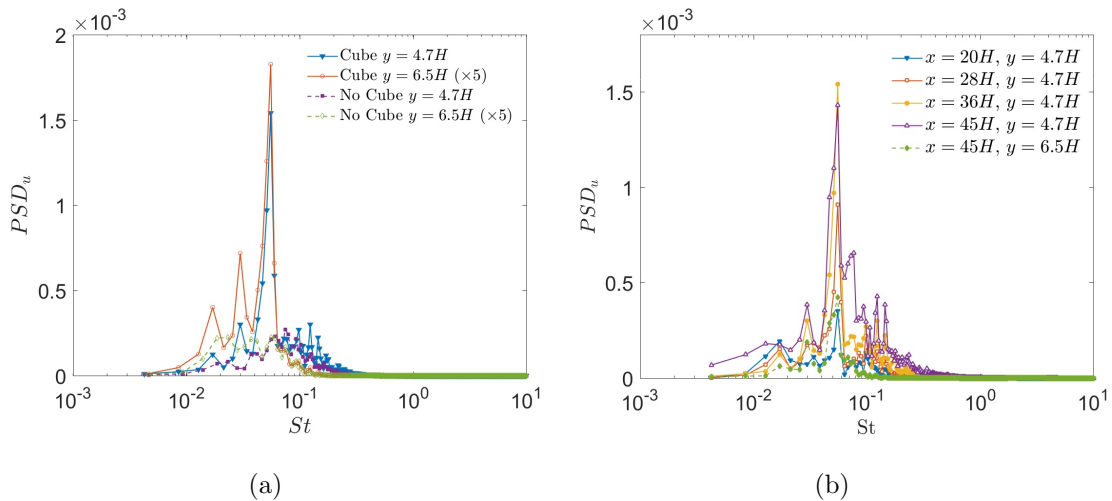
22

Figure 10: **a)** Span-averaged energy spectra of the streamwise component u. Comparison with and without cube at $x = 36H$, $y = 4.7H$ from the cube position (point P in Figure 9). **b)** Span-averaged temporal spectra of the streamwise velocity component, from the cube simulation, measured in the free-stream at several streamwise positions (points $A-D$ and D'). The non-dimensional PSD is defined as $PSD_u = E_{uu} U_\infty^{-1} H^{-1}$.

$St \approx 0.15 - 0.2$. However, this low frequency peak was only detected in the far-field spectra of high aspect ratio cylinders ($H/D > 9$, where D is the cylinder diameter), which is not the case here. Therefore, it is reasonable to think that the far-field peak in our simulations may not be related to a tip flow shedding but is otherwise connected to another physical phenomenon.

Figure 11 shows that the peak found in the energy spectra of the streamwise velocity component can also be found for the wall-normal component v. Moreover, the magnitude of the peak is of the same order for these two components. On the other hand, the energy spectra of the spanwise component does not seem to present a well-defined peak: a single frequency with significantly higher power spectral density cannot be clearly identified. Indeed, the maximum value in the w-component spectra at $x = 36H$, $y = 4.7H$ is about 15 times lower than the peak value found in the energy spectra of u and v. It suggests that the far-field velocity fluctuations are fundamentally two-dimensional in our simulations, which may possibly be explained by either of the

23

following reasons or the combination of them:

a) The large-scale fluctuations generated by the cube are two-dimensional themselves and might be unrelated to the shedding at $St = 0.15$ detected in the near-wall region, which generates spanwise fluctuations (see Figure 8(b)). The far-field fluctuations might be associated with spanwise-oriented vortices generated on top of the cube and/or with the turbulent interaction of the heads of the hairpin vortices observed behind the cube.

b) The scale of the far-field fluctuations is so large that it occupies the entire spanwise extent of the computational domain. The time separation of the structures associated with $St = 0.05$ is $\Delta t \approx 20H/U_\infty$ and if one assumes Taylor hypothesis (convection velocity equal to U_∞), the scale associated with such structures would be $20H$, larger that the spanwise extent $L_z = 10H$.
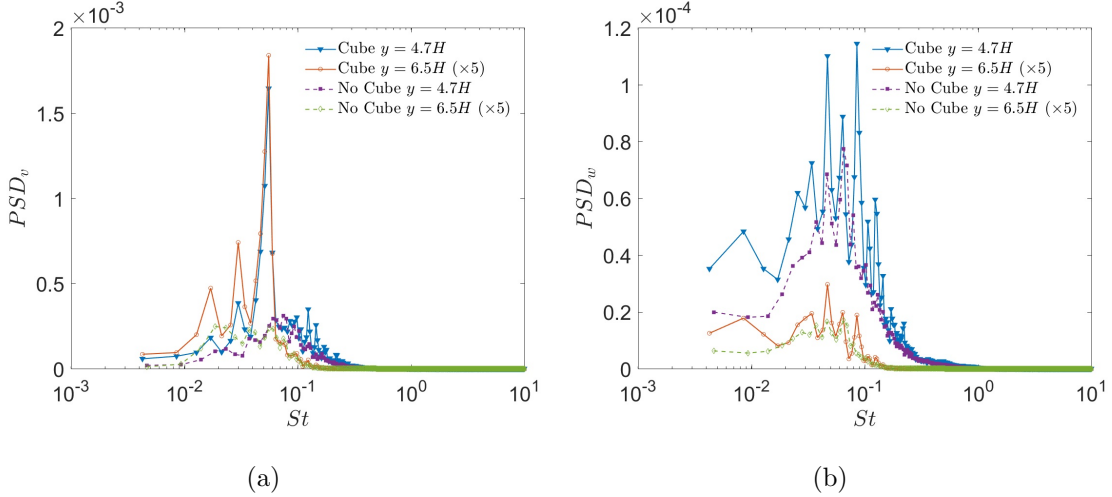

(a)   (b)

Figure 11: **a)** Span-averaged energy spectra of the wall-normal component v. Comparison with and without cube at $x = 36H$, $y = 4.7H$ from the cube position (point P in Figure 9) and $x = 36H$, $y = 6.5H$. **b)** Span-averaged energy spectra of the spanwise component w. Comparison with and without cube, also at $x = 36H$, $y = 4.7H$. The non-dimensional PSD is defined as $PSD_{u_i} = E_{u_i u_i} U_\infty^{-1} H^{-1}$.

The instantaneous streamwise velocity fluctuations, probed at $x = 45H$, $y = 6H$, $z = 0$ and plotted in Figure 12(a), show evident differences between the two TBL

simulations with and without the cube. The time-signal from the immersed-cube simulation presents higher maxima and minima and the separation between these peaks is relatively constant over time. This suggests that the cube is exciting or enhancing free-stream fluctuations at a particular low frequency, consistent with the peak location in the energy spectra.
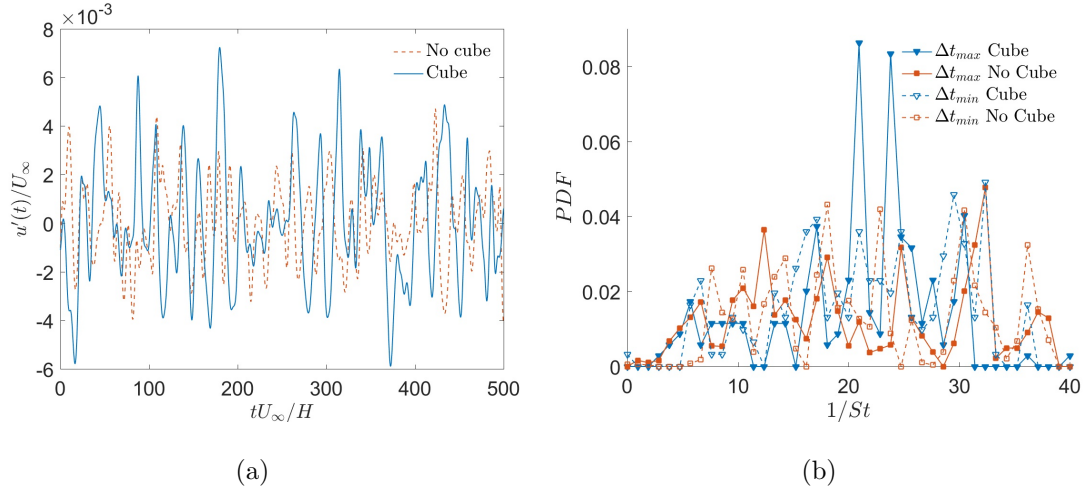

(a)

(b)

Figure 12: **a)** Time signal of the fuctuating streamwise velocity u', with and without the cube, at the position $x = 45H$, $y = 6H$. **b)** Probability distribution function (PDF) of the time lapse between velocity maxima (conditioned to $u' > 0.002$) and minima (conditioned to $u' < -0.002$), at the position $x = 45H$, $y = 6H$, $z = 0$.

To confirm this, the probability distribution function (PDF) of the time-lapse between maxima of u' (conditioned to $u' > 2 \times 10^{-3}$) was computed at $x = 45H$, $y = 6H$. This PDF shows that the events with time such that $\Delta t \approx 20H/U_\infty$, equivalent to the frequency $St = 0.05$, have a high probability peak of approximately 8% when the cube is present (Figure 12(b)). The PDF of the time-lapse between local minima (conditioned to $u' < -2 \times 10^{-3}$) does not show such high peaks at $\Delta t \approx 20H/U_\infty$, supporting existing evidence of high skewness in the velocity signal at this location.

The sharp peak described in this section is not observed in the simulations of a cube immersed in a LBL. This suggest that the far-field structures responsible for this peak is only generated when the cube interacts with an incoming turbulent boundary layer.

25

The comparison between these two configurations revealed that some flow structures in the cube near-field are fundamentally different, even if the Reynolds number is the same ($Re_H = 3,000$). For instance, we previously discussed the differences between the mean-flow features around the cube and mentioned that the horseshoe vortex system in front of the cube is unstable only in the TBL simulation.

5. Conclusions

The interaction between a turbulent boundary layer and a wall-attached cube generates a low-frequency sharp peak in the far-field energy spectra which persists for long downstream distances with a constant Strouhal number $St = 0.05$. This peak is not due to numerical effects nor related to the background boundary layer turbulence, since it was not identified in the unperturbed zero-pressure gradient turbulent boundary layer. The Strouhal number of this peak does not correspond to the vortex shedding detected close to the cube at $St = 0.14$, hence it might be associated with an additional phenomenon. The peak has been observed in the energy spectra of the streamwise and vertical fluctuating velocity components but not in the spectra of the spanwise fluctuations, which suggests that the responsible flow structures might be essentially two-dimensional.

A series of simulations with incoming laminar boundary layer conditions investigated the coherent structures generated by the cube at different Reynolds numbers, in the range $Re_H = 500 - 3,000$. The coherent structures are mainly organised in two distinct vortex streets: hairpin vortices shed from the top of the cube and wall-attached hairpin vortices generated at both sides of the cube wake. This study revealed that there is a strong Reynolds number dependence for the peaks found in the energy spectra, but the far-field peak was not found in those simulations with incoming laminar conditions.

The turbulent upstream conditions are therefore related, directly or indirectly, to the far-field peak. For this reason, the origin of the far-field peak is most probably related to mechanisms involving the interaction between a turbulent boundary layer and a cube. The energy spectra of the incoming boundary layer at $y = 4.7H$ has a broad

26

peak centred around $St = 0.07 - 0.1$. The interaction with the cube might modulate or amplify the oscillations at $St = 0.05$ and this modulation could be responsible for the far-field peak, since the low frequency velocity fluctuations are weakly dissipated by viscous stresses.

As explained before, the flow dynamics around the cube present some fundamental differences between the LBL and TBL simulations at $Re_H = 3000$. For instance, the main mean-flow recirculations, behind and on top of the cube, are not completely developed in the LBL simulation. Secondly, the horseshoe vortex system in front of the cube is stable with 8 vortices in the LBL simulation and unstable in the TBL simulation.

The authors of Yakhot et al. (2006a) suggested that the unstable horseshoe vortex system has a similar dynamic as the inviscid-viscous interaction between a vortex and the high-vorticity region near the wall in a junction flow. They described the unsteady mechanism in front of the cube as a quasi-periodic regeneration of the horseshoe vortex and a low-momentum fluid ejection away from the wall. The dominant frequency of this cycle is reported to be at $St = 0.08$. It is unclear whether the ejection of low-momentum fluid at such low frequencies might be related to the velocity fluctuations at $St = 0.05$ found in the far-field of our simulation with a turbulent incoming boundary layer. Both phenomena are presumably only found at high Reynolds numbers when the flow around the cube is fully turbulent.

6. Acknowledgement

₅₃₅ **References**

Adrian, R. J. (2007). Hairpin vortex organization in wall turbulence. *Physics of Fluids*, *19*, 041301.

Baker, C. J. (1979). The laminar horseshoe vortex. *Journal of Fluid Mechanics*, *95*, 347–367.

₅₄₀ Becker, S., Hahn, C., Kaltenbacher, M., & Lerch, R. (2008). Flow-induced sound of wall-mounted cylinders with different geometries. *AIAA Journal*, *46*, 2265–2281.

Castro, I., & Robins, A. (1977). The flow around a surface-mounted cube in uniform and turbulent streams. *Journal of Fluid Mechanics*, *79*, 307–335.

Corke, T., Nagib, H., & Tan-Atichat, J. (1979). Flow near a building model in a ₅₄₅ family of surface layers. *Journal of Wind Engineering and Industrial Aerodynamics*, *5*, 139–158.

Diaz-Daniel, C., Laizet, S., & Vassilicos, J. (2017). Wall shear stress fluctuations: mixed scaling and their effects on velocity fluctuations in a turbulent boundary layer. *Physics of Fluids*, *29*, 055102.

₅₅₀ van Dijk, A., & de Lange, H. (2007). Compressible laminar flow around a wall-mounted cubic obstacle. *Computers & Fluids*, *36*, 949–960.

Favre, A., Gaviglio, J., & Dumas, R. (1957). Space-time double correlations and spectra in a turbulent boundary layer. *Journal of Fluid Mechanics*, *2*, 313–342.

Hearst, R. J., Gomit, G., & Ganapathisubramani, B. (2016). Effect of turbulence on ₅₅₅ the wake of a wall-mounted cube. *Journal of Fluid Mechanics*, *804*, 513–530.

Hunt, J. C. R., Wray, A. A., & Moin, P. (1988). Eddies, stream, and convergence zones in turbulent flows. In *Proceedings of the 1988 Summer Program (SEE N89-24538)* (pp. 193–208). NASA Center for Turbulence Research, Stanford, USA.

Hwang, J.-Y., & Yang, K.-S. (2004). Numerical study of vortical structures around a wall-mounted cubic obstacle in channel flow. *Physics of Fluids*, *16*, 2382–2394.

Jiménez, J., Hoyas, S., Simens, M. P., & Mizuno, Y. (2010). Turbulent boundary layers and channels at moderate Reynolds numbers. *Journal of Fluid Mechanics*, *657*, 335–360.

Kawamura, T., Hiwada, M., Hibino, T., Mabuchi, I., & Kumada, M. (1984). Flow around a finite circular cylinder on a flat plate: Cylinder height greater than turbulent boundary layer thickness. *Bulletin of JSME*, *27*, 2142–2151.

King, W., & Pfizenmaier, E. (2009). An experimental study of sound generated by flows around cylinders of different cross-section. *Journal of Sound and Vibration*, *328*, 318–337.

Laizet, S., & Lamballais, E. (2009). High-order compact schemes for incompressible flows: A simple and efficient method with quasi-spectral accuracy. *Journal of Computational Physics*, *228*, 5989–6015.

Laizet, S., & Li, N. (2011). Incompact3d : A powerful tool to tackle turbulence problems with up to $O(10^5)$ computational cores. *International Journal for Numerical Methods in Fluids*, *67*, 1735–1757.

Li, Q., Hu, G., & Yan, B.-W. (2014). Investigation of the effects of free-stream turbulence on wind-induced responses of tall building by large eddy simulation. *Wind and Structures*, *18*, 599–618.

Li, W. W., & Meroney, R. N. (1983). Gas dispersion near a cubical model building. Part I. Mean concentration measurements. *Journal of Wind Engineering and Industrial Aerodynamics*, *12*, 15–33.

Liakos, A., & Malamataris, N. A. (2014). Direct numerical simulation of steady state, three dimensional, laminar flow around a wall mounted cube. *Physics of Fluids*, *26*, 053603.

29

Martinuzzi, R., & Havel, B. (2004). Vortex shedding from two surface-mounted cubes in tandem. *International Journal of Heat and Fluid Flow*, *25*, 364–372.

Martinuzzi, R., & Tropea, C. (1993). The Flow Around Surface-Mounted, Prismatic Obstacles Placed in a Fully Developed Channel Flow. *Journal of Fluids Engineering*, *115*, 85–92.

Mavroidis, I., Griffiths, R., & Hall, D. (2003). Field and wind tunnel investigations of plume dispersion around single surface obstacles. *Atmospheric Environment*, *37*, 2903–2918.

McClean, J., & Sumner, D. (2014). An experimental investigation of aspect ratio and incidence angle effects for the flow around surface-mounted finite-height square prisms. *ASME. Journal of Fluids Engineering*, *136*, 081206–081206–10.

Meinders, E., Hanjalic, K., & Martinuzzi, R. (1999). Experimental study of the local convection heat transfer from a wall-mounted cube in turbulent channel flow. *Journal of Heat Transfer*, *121*, 564–573.

Monnier, B., Neiswander, B., & Wark, C. (2010). Stereoscopic particle image velocimetry measurements in an urban-type boundary layer: Insight into flow regimes and incidence angle effect. *Boundary-Layer Meteorology*, *135*, 243–268.

Moreau, D. J., & Doolan, C. J. (2013). Flow-induced sound of wall-mounted finite length cylinders. *AIAA journal*, *51*, 2493–2502.

Ogawa, Y., Oikawa, S., & Uehara, K. (1983). Field and wind tunnel study of the flow and diffusion around a model cube.-I. Flow measurements. *Atmospheric Environment (1967)*, *17*, 1145 –1159.

Park, C.-W., & Lee, S.-J. (2000). Free end effects on the near wake flow structure behind a finite circular cylinder. *Journal of Wind Engineering and Industrial Aerodynamics*, *88*, 231–246.

30

Philips, O. (1955). The irrotational motion outside a free turbulent boundary. *Mathematical Proceedings of the Cambridge Philosophical Society*, *51*, 220–229.

Porteous, R., Doolan, C. J., & Moreau, D. J. (2013). Directivity pattern of flow-induced noise from a wall-mounted, finite length circular cylinder. In *Proceedings of Acoustics 2013, Annual Conference of the Australian Acoustical Society*. Victor Harbour, SA.

Porteous, R., Moreau, D. J., & Doolan, C. (2014). A review of flow-induced noise from finite wall-mounted cylinders. *Journal of Fluids and Structures*, *51*, 240–254.

Rodríguez-López, E., Bruce, P. J. K., & Buxton, O. R. H. (2016). On the formation mechanisms of artificially generated high reynolds number turbulent boundary layers. *Boundary-Layer Meteorology*, *160*, 1–24.

Rossi, R., Philips, D., & Iaccarino, G. (2010). A numerical study of scalar dispersion downstream of a wall-mounted cube using direct simulations and algebraic flux models. *International Journal of Heat and Fluid Flow*, *31*, 805–819.

Saeedi, M., LePoudre, P. P., & Wang, B.-C. (2014). Direct numerical simulation of turbulent wake behind a surface-mounted square cylinder. *Journal of Fluids and Structures*, *51*, 20–39.

Saha, A. K. (2013). Unsteady flow past a finite square cylinder mounted on a wall at low reynolds number. *Computers & Fluids*, *88*, 599–615.

Sakamoto, H., & Arie, M. (1983). Vortex shedding from a rectangular prism and a circular cylinder placed vertically in a turbulent boundary layer. *Journal of Fluid Mechanics*, *126*, 147–165.

Sakamoto, H., Moriya, M., Taniguchi, S., & Arie, M. (1982). The Form Drag of Three-Dimensional Bluff Bodies Immersed in Turbulent Boundary Layers. *Journal of Fluids Engineering*, *104*, 326–333.

31

Sakamoto, H., & Oiwake, S. (1984). Fluctuating Forces on a Rectangular Prism and a Circular Cylinder Placed Vertically in a Turbulent Boundary Layer. *Journal of Fluids Engineering*, *106*, 160–166.

Schlatter, P., & Örlü, R. (2010). Assessment of direct numerical simulation data of turbulent boundary layers. *Journal of Fluid Mechanics*, *659*, 116–126.

Schlatter, P., & Örlü, R. (2012). Turbulent boundary layers at moderate Reynolds numbers: inflow length and tripping effects. *Journal of Fluid Mechanics*, *710*, 5–34.

Sumner, D., Rostamy, N., Bergstrom, D., & Bugg, J. (2015). Influence of aspect ratio on the flow above the free end of a surface-mounted finite cylinder. *International Journal of Heat and Fluid Flow*, *56*, 290–304.

Sumner, D., Rostamy, N., Bergstrom, D., & Bugg, J. D. (2017). Influence of aspect ratio on the mean flow field of a surface-mounted finite-height square prism. *International Journal of Heat and Fluid Flow*, *65*, 1–20.

Vinuesa, R., Schlatter, P., Malm, J., Mavriplis, C., & Henningson, D. S. (2015). Direct numerical simulation of the flow around a wall-mounted square cylinder under various inflow conditions. *Journal of Turbulence*, *16*, 555–587.

Wang, H. F., Cao, H. L., & Zhou, Y. (2014a). POD analysis of a finite-length cylinder near wake. *Experiments in Fluids*, *55*, 1790.

Wang, H. F., & Zhou, Y. (2009). The finite-length square cylinder near wake. *Journal of Fluid Mechanics*, *638*, 453–490.

Wang, H. F., Zhou, Y., Chan, C. K., & Lam, K. S. (2006). Effect of initial conditions on interaction between a boundary layer and a wall-mounted finite-length-cylinder wake. *Physics of Fluids*, *18*, 065106.

Wang, L., & Lu, X.-Y. (2012). Flow topology in compressible turbulent boundary layer. *Journal of Fluid Mechanics*, *703*, 255–278.

Wang, Y., Jackson, P., & Sui, J. (2014b). Simulation of turbulent flow around a surface-mounted finite square cylinder. *Journal of Thermophysics and Heat Transfer*, *28*, 118–132.

Yakhot, A., Anor, T., Liu, H., & Nikitin, N. (2006a). Direct numerical simulation of turbulent flow around a wall-mounted cube: spatio-temporal evolution of large-scale vortices. *Journal of Fluid Mechanics*, *566*, 1–9.

Yakhot, A., Liu, H., & Nikitin, N. (2006b). Turbulent flow around a wall-mounted cube: A direct numerical simulation. *International Journal of Heat and Fluid Flow*, *27*, 994–1009.

Yanaoka, H., Inamura, T., & Kawabe, S. (2007). Turbulence and heat transfer of a hairpin vortex formed behind a cube in a laminar boundary layer. *Numerical Heat Transfer, Part A: Applications*, *52*, 973–990.